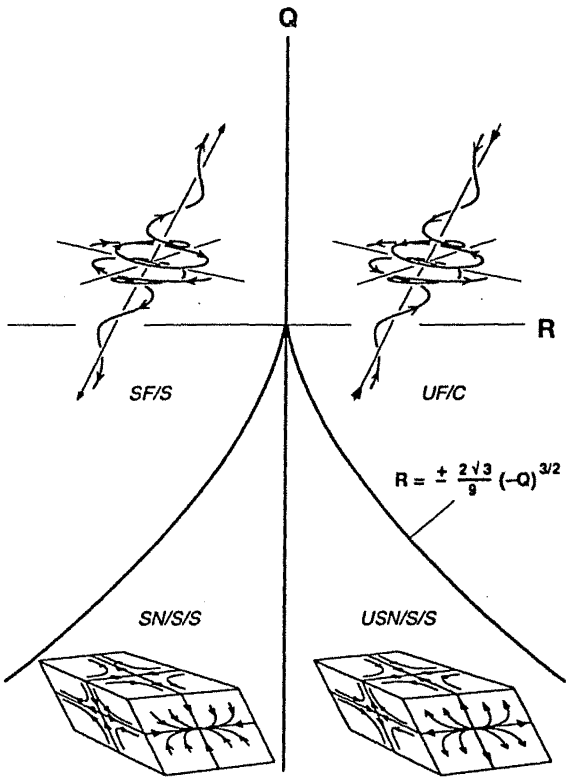

FIGURE 1. Local non-degenerate topologies in the $Q-R$ plane. *SF/S: stable focus/stretching, UF/C: unstable focus/contracting, $SN/S/S$: stable node/saddle/saddle* and *$USN/S/S$: Unstable node/saddle/saddle.*

Biot-Savart law and in no way depend on the above relative strengths. Whether or not a region of vorticity is focal depends on the rate of strain environment in which it is embedded and so also do all definitions for a vortex core. Nevertheless it is felt that most if not all of the attached eddies should display extensive focal regions as a result of the work of Blackburn, Mansour & Cantwell (1996), who examined the data from channel flow computations of Kim (1989). Here focal regions were found to exist in tubes, some of which extended from very close to the wall to the center plane of the channel. The authors consider these to be the clearest and most spectacular indicators of eddying motions so far seen in DNS data and at first sight look like the attached eddies envisaged by Perry and Chong (1982).

Following Chong, Perry & Cantwell (1989, 1990), the geometry of the streamline pattern at any point in the flow, as seen by a non-rotating observer moving with the velocity of that point, can be classified by studying certain invariants of the velocity gradient tensor $A_{ij} = \partial u_i/\partial x_j$ at that point. Here u_i is the velocity vector and x_i is the space vector. The characteristic equation of A_{ij} is

$$\lambda^3 + P\lambda^2 + Q\lambda + R = 0 \tag{1}$$

where P, Q and R are the tensor invariants. These are

$$P = -trace(\mathbf{A}) \tag{2}$$

$$Q = \frac{1}{2}(P^2 - trace(\mathbf{A}^2)) \tag{3}$$

and

$$R = -det(\mathbf{A}). \tag{4}$$

For incompressible flow, $P = 0$ from continuity and so

$$\lambda^3 + Q\lambda + R = 0. \tag{5}$$

The eigenvalues λ which determine the topology of the local flow pattern are determined by the invariants R and Q. In fact the $R - Q$ plane, shown in Fig. 1, is divided into regions according to flow topology.

The discriminant of A_{ij} is defined as

$$D = \frac{27}{4}R^2 + Q^3 \tag{6}$$

and the boundary dividing flows with complex eigenvalues from real is

$$D = 0 \tag{7}$$

Figure 2 shows contours of D on the $R - Q$ plane. For $D > 0$, Eq. (5) admits two complex and one real solution for λ. Such points are called foci and are part of the focal regions mentioned earlier. If $D < 0$, all 3 solutions for λ are real and the associated pattern is referred to as a node-saddle-saddle point according to the terminology adopted by Chong *et al.* (1990).

As implied earlier, the velocity gradient tensor can be split into two components thus:

$$A_{ij} = S_{ij} + W_{ij} \tag{8}$$

where S_{ij} is the symmetric rate of strain tensor and W_{ij} is the skew symmetric rate of rotation tensor. These are given by

$$S_{ij} = \frac{1}{2}(\frac{\partial u_i}{\partial x_j} + \frac{\partial u_j}{\partial x_i}) \tag{9}$$

and

$$W_{ij} = \frac{1}{2}(\frac{\partial u_i}{\partial x_j} - \frac{\partial u_j}{\partial x_i}). \tag{10}$$

The invariants of S_{ij} are P_s, Q_s, and R_s and are defined in an analogous way as the invariants of A_{ij}. For incompressible flow $P_s = 0$,

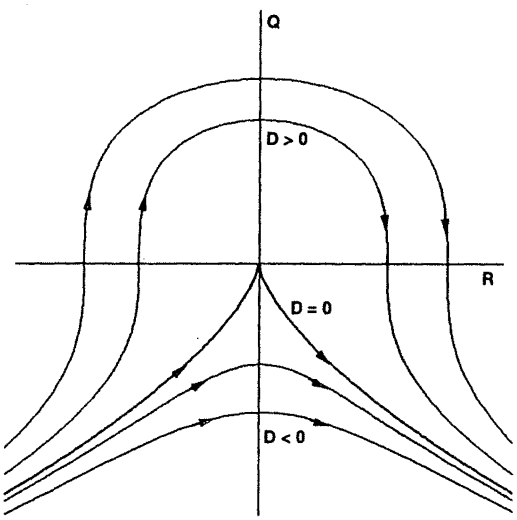

FIGURE 2. Trajectories of constant D in the $R-Q$ plane.

$$Q_s = -\frac{1}{2}S_{ij}S_{ij} \tag{11}$$

and

$$R_s = -\frac{1}{3}S_{ij}S_{jk}S_{ki} \tag{12}$$

The corresponding invariants of W_{ij} are P_w, Q_w and R_w. $P_w = R_w = 0$ but Q_w is non zero and is given by

$$Q_w = \frac{1}{2}W_{ij}W_{ij} \tag{13}$$

and is proportional to the enstrophy density. Other relations of interest are

$$\phi = 2\nu S_{ij}S_{ij} = -4\nu Q_s \tag{14}$$

where ϕ is the dissipation of kinetic energy into heat per unit mass and it should be noted that Q_s is always a negative quantity.

It can be shown that

$$Q = Q_w + Q_s = \frac{1}{2}(W_{ij}W_{ij} - S_{ij}S_{ij}) \tag{15}$$

According to the work of Viellefosse (1982, 1984) and the more recent work of Cantwell (1992), the evolution of the velocity gradient tensor A_{ij} for a fluid particle is given by the following :

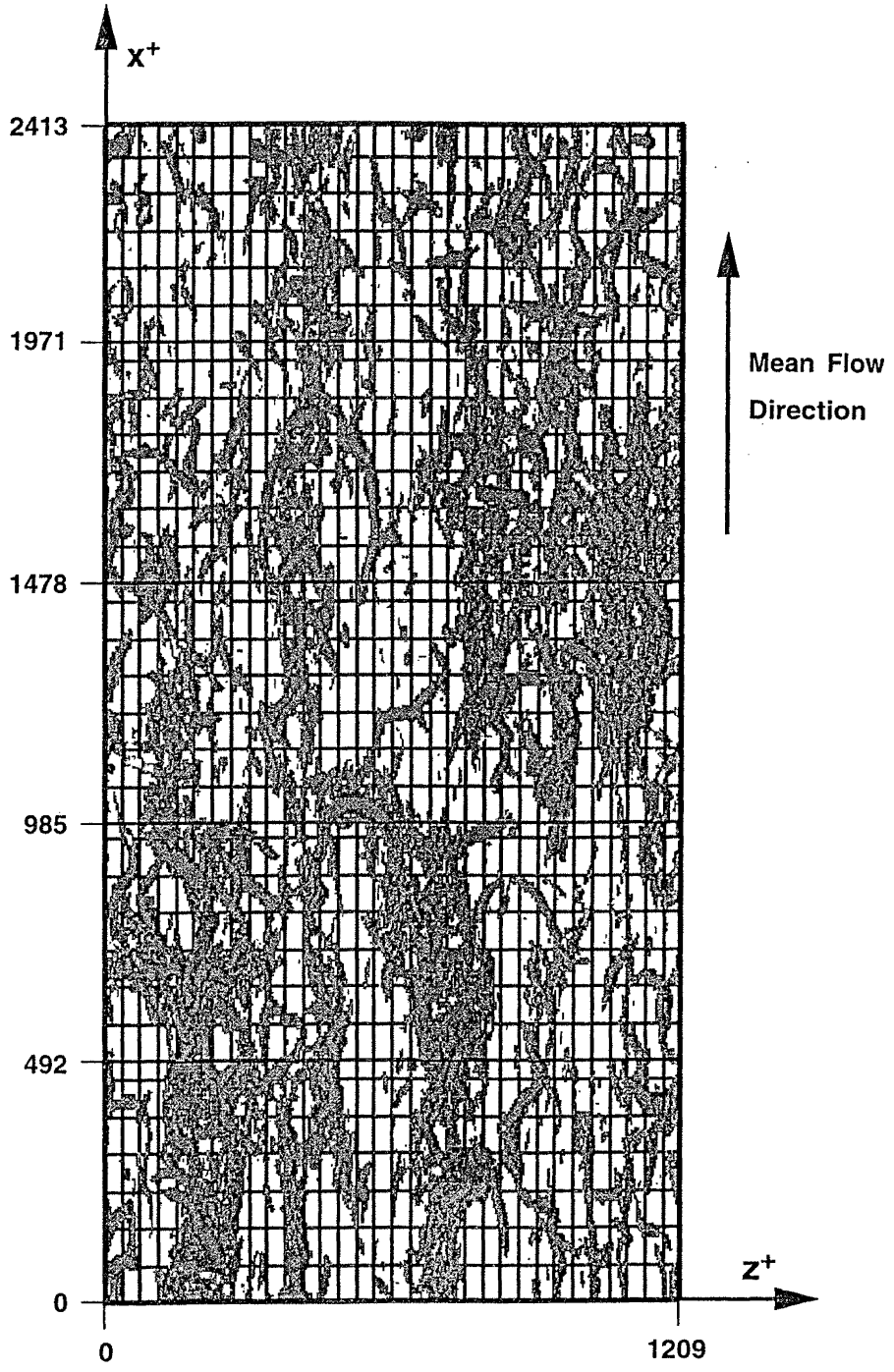

FIGURE 3. Isosurfaces of discriminant ($D \approx 0$) for zero pressure gradient data of Spalart for $Re_\theta = 670$ (from Chacin *et al.* (1996)).

$$\frac{\partial A_{ij}}{\partial t} + u_k \frac{\partial A_{ij}}{\partial x_k} + A_{ik}A_{kj} - A_{km}A_{mk}\frac{\delta_{ij}}{3} = H_{ij} \tag{16}$$

Here δ_{ij} is the Kronecker delta and

$$H_{ij} = -\left(\frac{\partial^2 p}{\partial x_i \partial x_j} - \frac{\partial^2 p}{\partial x_k \partial x_k}\frac{\delta_{ij}}{3}\right) + \nu \frac{\partial^2 A_{ij}}{\partial x_k \partial x_k} \tag{17}$$

If the viscous term and the pressure Hessian terms are small, the evolution of A_{ij} for fluid particles follows the so called restricted Euler equation, and solution trajectories of such particles follow the contours of constant D on the $R-Q$ plane as shown in Fig. 2. It is thought that this might be an appropriate description of the motions for fine scale eddies at high Reynolds numbers. It is found here that this restricted Euler equation is not valid for the Spalart (1988) data, which is of course at low Reynolds number. However, computations show that once a particle is focal it is highly probable it will remain focal. This study of particle trajectories on the $R-Q$ plane gives us a first glimpse of how fluid dynamics might be combined with the usual kinematic description of eddy structures as has been used in the attached eddy hypothesis.

It has been pointed out that three-dimensional plots of vortex lines or particle trajectories are extremely complex and confusing and not very helpful in gaining an insight into eddying motions (Cantwell (1979)). However, a very interesting feature of the isosurfaces of constant D found by Blackburn *et al.* (1996) is that they enclose a rather concentrated and well-ordered bundle of vortex lines. Finally, Blackburn *et al.* found that isosurfaces of constant D were superior to isosurfaces of enstrophy density or dissipation of kinetic energy for showing clear, well defined structures. The authors do not fully understand why this should be and this is a question which needs to be pursued in future work.

2. Results

2.1 Normalization of the discriminant

The raw values of the discriminant D were used in the case of the Spalart DNS data without any additional normalization. In the case of the Na & Moin DNS data, it is assumed that the inflow free-stream velocity is unity and that all length scales in the database are normalized by δ^*_{in}, the displacement thickness of the inflow boundary layer. The computed raw values of D were normalized by a velocity gradient representative of the mean separation bubble flow to the power of 6. This resulted in the raw values of D being multiplied by a factor of 10^6, and so maximum values of normalized D were of order 10^6. Typical values of D used in the isosurface visualization of D were of the order of $1 - 10$.

2.2 Zero pressure gradient boundary layer

Figure 3 shows a very clear picture (from Chacin *et al.* 1996) of isosurfaces of the discriminant for part of the Spalart (1988), $Re_\theta = 670$, zero pressure gradient turbulent boundary layer simulation data. Some Theodorsen-type vortices are apparent

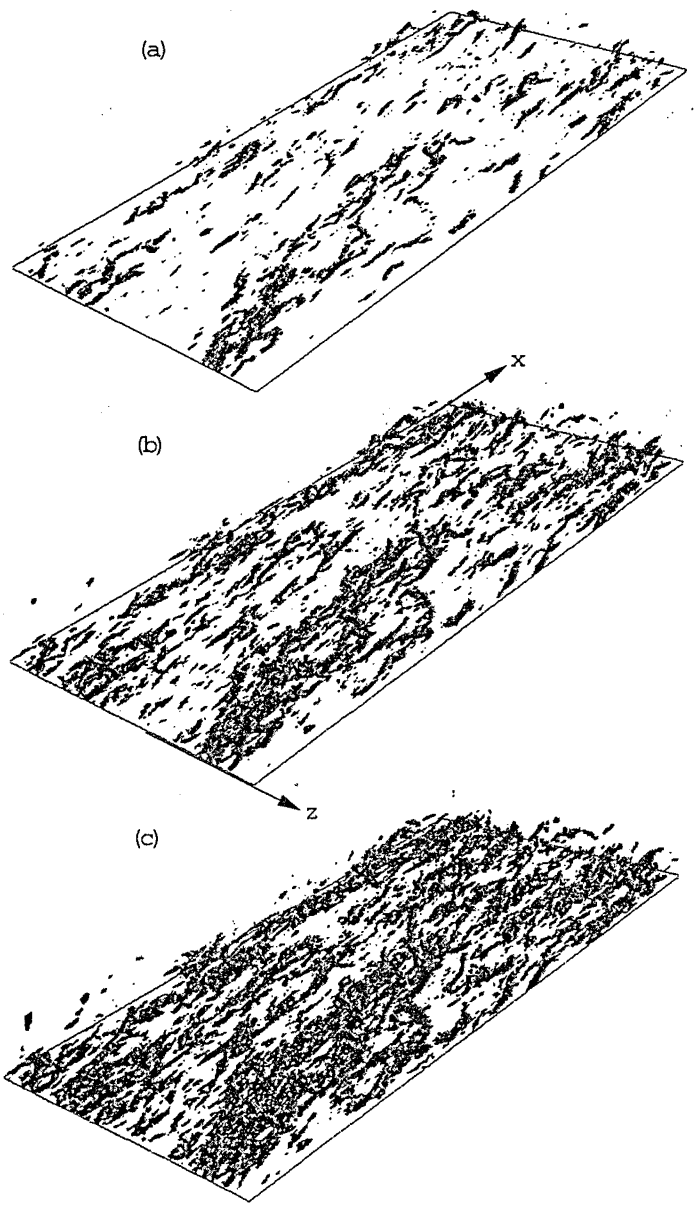

FIGURE 4. Isosurface of constant discriminant, D, for zero pressure gradient turbulent boundary layer flow at $R_\theta = 670$ for different threshold values of (a) $D = 1.0$, (b) $D = 0.25$ and (c) $D = 0.1$. The displayed boundary layer structures cover $\Delta x^+ = 2442$, $y^+_{min} = 6.4$, $y^+_{max} = 375$ and $\Delta z^+ = 1221$. Here $^+$ denotes viscous lengths.

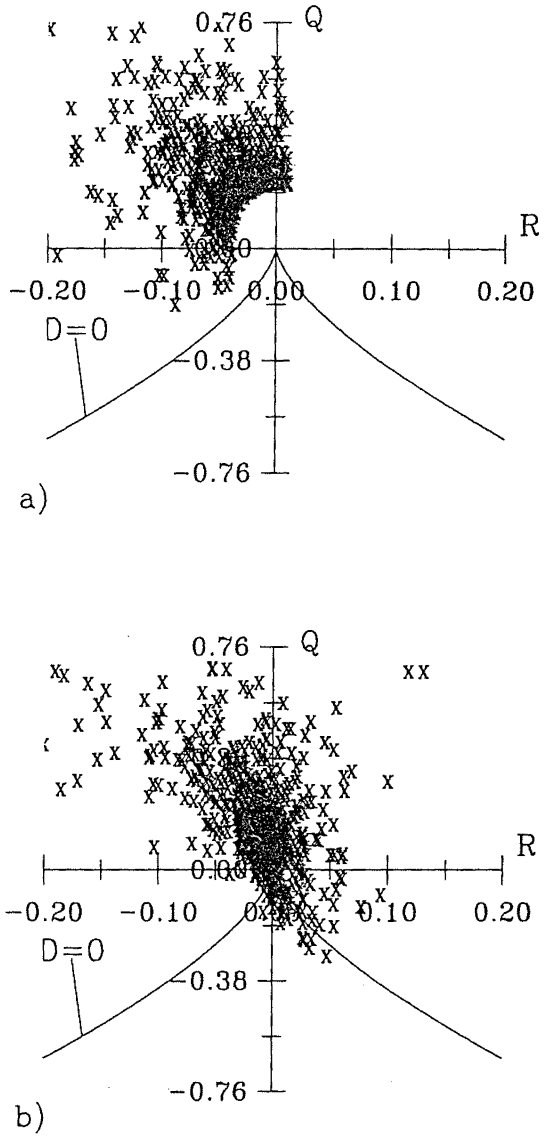

FIGURE 5. Particle trajectories on the $R - Q$ plane computed from the zero pressure gradient turbulent boundary layer data of Spalart (1988).

together with intertwining tubes forming braids which are near the surface and are aligned with the streamwise direction. Figures 4(a), (b), and (c) show the same flow case of Spalart but for a different time frame covering a larger field of data. The figures are ordered for diminishing values of D. Figure 4(a) shows structures which could be interpreted as $\cap$ or Λ eddies when viewed from upstream. These loops appear to lean in the streamwise direction. As the "threshold" is reduced (i.e. as the value of D for the isosurface is reduced), more attached vortex loops become apparent, but the picture becomes confusing. The structures are not as smooth as

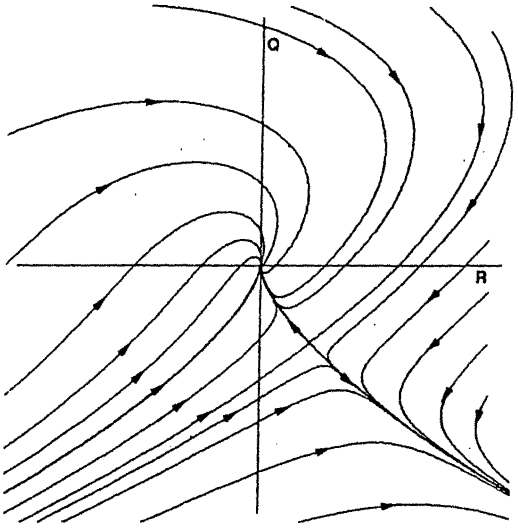

FIGURE 6. Particle trajectories using a linear diffusion model for H_{ij} of Martin & Dopazo (1995).

the Chacin *et al.* (1996) data, and this is because of computer storage problems. There is nonetheless a suggestion of Theodorsen type structures with focal tubes coming down to the wall and running along it in the streamwise direction. Superposition of vortex lines (done at the computer terminal) is confusing, but they tend to loop and lean in the streamwise direction in a manner similar to the isosurfaces of D.

Particle trajectories on the $R-Q$ plane show that there is a rapid convergence to small but positive D. Figure 5 shows a typical calculation for a selection of particles with $D > 0$ at the initial time. These particles are identified at $t = 0$ and then followed in space as the DNS code is run forward in time for several eddy characteristic turnover times. These calculations show that once a particle has a positive discriminant (i.e. once it is focal), it has a high probability of remaining focal over several eddy turnover times. Various models for the H_{ij} term are currently being formulated. One recent model by Martin & Dopazo (1995) shows ensemble averaged $R-Q$ trajectories with the topology sketched in Fig. 6, and this is consistent with the above findings. Time evolution computations and animations of the isosurfaces of the discriminant show that such surfaces retain their shape and identity for considerable streamwise distances. When viewing a movie made up of successive frames, these structures appear to convect downstream in close accordance with Taylor's hypothesis. Smaller structures close to the wall appear to be convecting at smaller velocities than the larger structures further away from the wall. All of this is consistent with aspects of the attached eddy model discussed by Perry *et al.* (1986).

In zero pressure gradient layers, there seems to be a strong link between these attached eddies and the Reynolds shear stress. Perry and Chong (1982) showed that

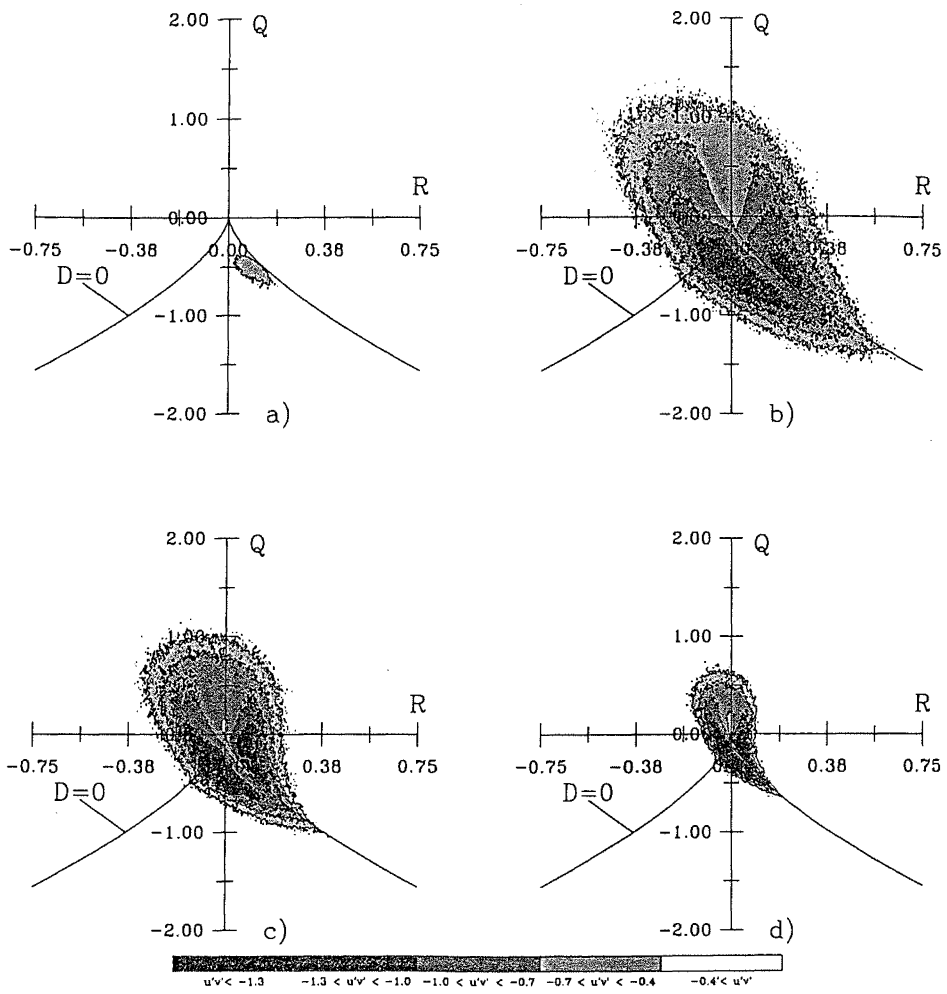

FIGURE 7. Time-averaged values of $-u'v'$ for zero pressure gradient turbulent boundary layer flow with $Re_\theta = 670$ in (a) viscous sub-layer $y^+ < 5.0$ (b) buffer layer, $5.0 < y^+ < 41$, (c) logarithmic region, $41 < y^+ < 107$ and (d) wake region, $y^+ > 107$. The contour levels shown are normalized by u_τ^2.

it is likely that they contribute almost entirely to the mean vorticity distribution and the Reynolds shear stress distribution. Figure 7 shows that peaks in the time-averaged values of $-u'v'$ occur near to and on either side of the contour $D = 0$ on the $R > 0$ branch of the $R - Q$ plane. Here u' and v' are the streamwise and wall-normal components of the velocity fluctuations respectively.

Chacin *et al.* (1996) found that the contributions to the Reynolds shear stress by an attached eddy come from regions close in physical space to the isosurface of D, which is small and positive as seen in Fig. 9 of that reference. They found that high Reynolds stress events are strongly correlated with changes in sign of the discriminant. This is important near the wall where the discriminant and the

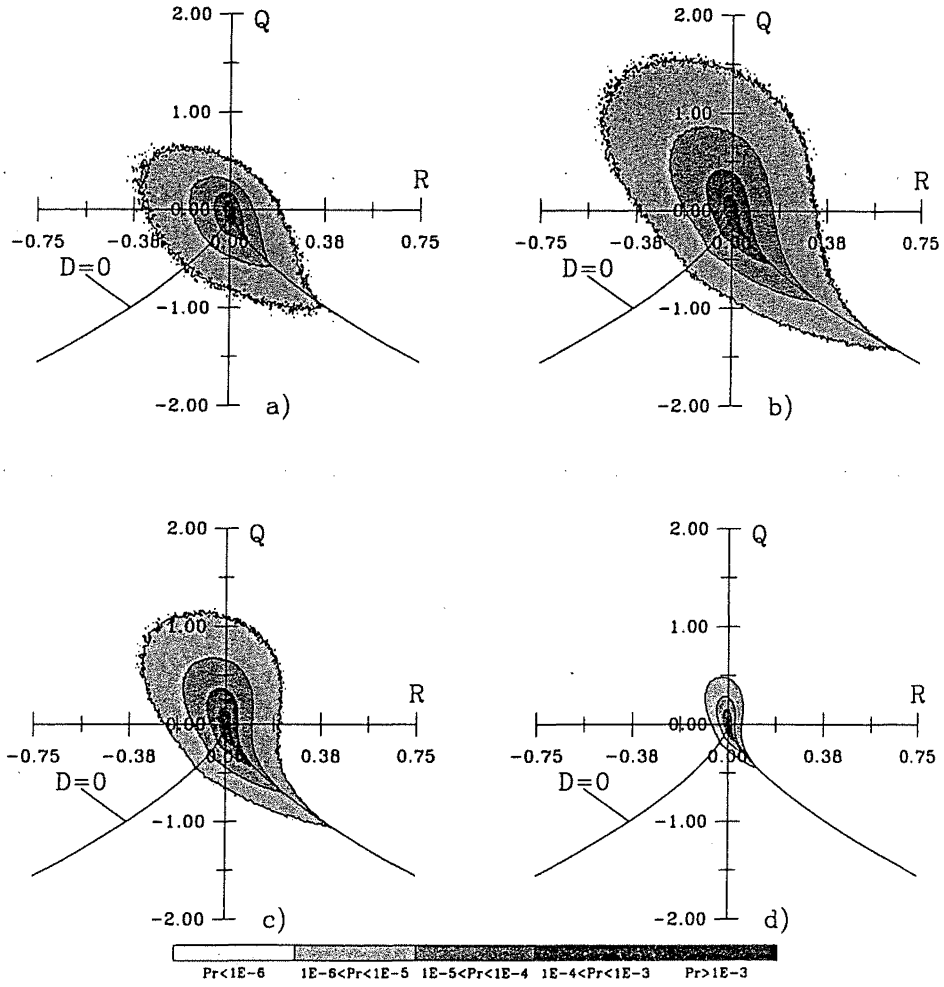

FIGURE 8. Joint probability density function between Q and R for zero pressure gradient turbulent boundary layer flow with $R_\theta = 670$ in (a) viscous sub-layer $y^+ < 5.0$ (b) buffer layer, $5.0 < y^+ < 41$, (c) logarithmic region, $41 < y^+ < 107$ and (d) wake region, $y^+ > 107$.

vorticity have completely different character. The role of the discriminant needs to be clarified. One approach would be to analyze the velocity gradient tensor induced by artificial isolated eddies of various shapes using the Biot-Savart law in the manner of Perry and Marusic (1995).

Figures 8, 9, 10, and 11 show joint probability distribution diagrams of the various topological invariants. On these diagrams are shown contours of the joint pdf's of various pairs of quantities. Figure 8 shows the joint pdf's of R and Q and Figs. 8(a) through to 8(d) show results for the sublayer, buffer zone, logarithmic region, and wake region respectively. Figure 9 shows the joint pdf of R_s and Q_s. In the sublayer, Fig. 9(a) shows that most of the rate of strain is two dimensional, since the data

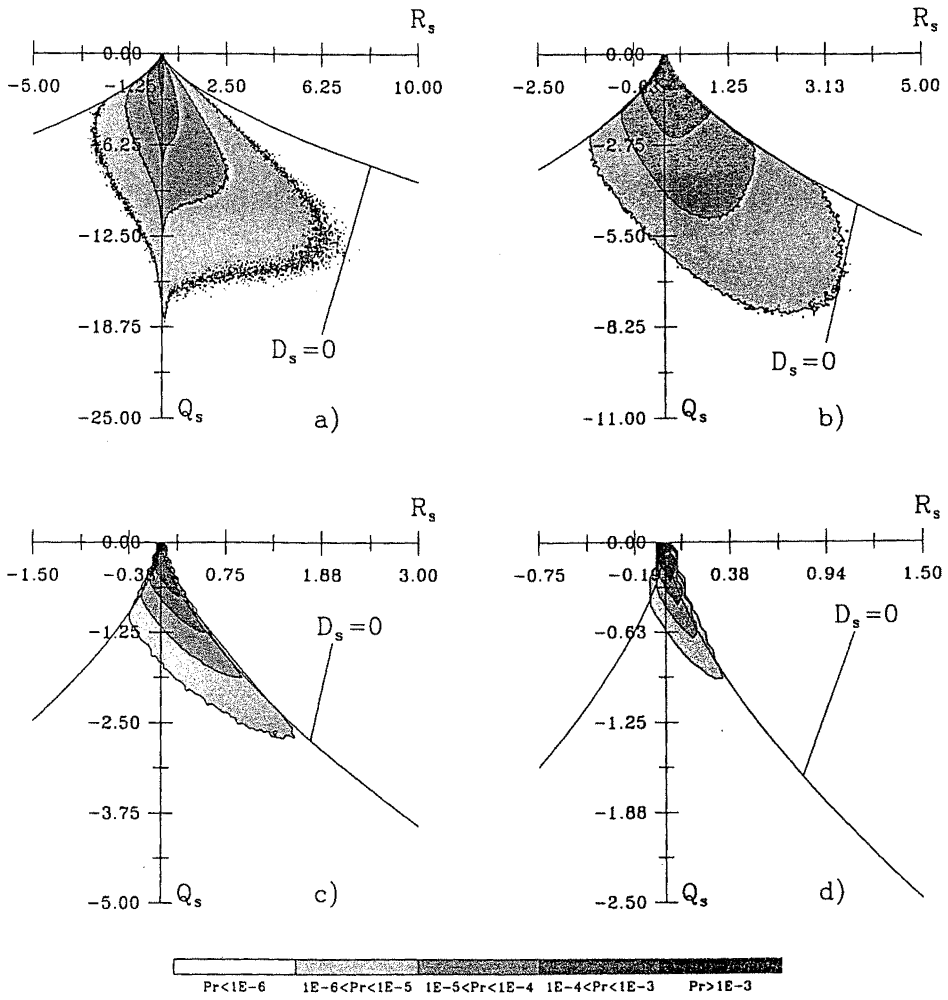

FIGURE 9. Joint probability density function between Q_S and R_S for zero pressure gradient turbulent boundary layer flow with $R_\theta = 670$ in (a) viscous sub-layer $y^+ < 5.0$ (b) buffer layer, $5.0 < y^+ < 41$, (c) logarithmic region, $41 < y^+ < 107$ and (d) wake region, $y^+ > 107$.

collects along the Q_s axis and very high Q_s values are encountered. In the buffer zone results shown in Fig. 9(b) there is a drift towards $D = 0$, and $|Q_s|$ is half that of the sublayer. In Fig. 9(c), the logarithmic region, there is a further decrease in $|Q_s|$ and further movement towards the $D = 0$ contour. The rate of strain is very three dimensional. In the wake region shown in Fig. 9(d), $|Q_s|$ is orders of magnitude smaller than the other regions and very little dissipation is occurring there.

Figure 10 shows the joint pdf between $-Q_s$ and Q_w. A line of 45° through the origin is symptomatic of vortex sheet behavior or two-dimensional shearing. Data running close to the Q_w axis could be interpreted as belonging to vortex tubes, and

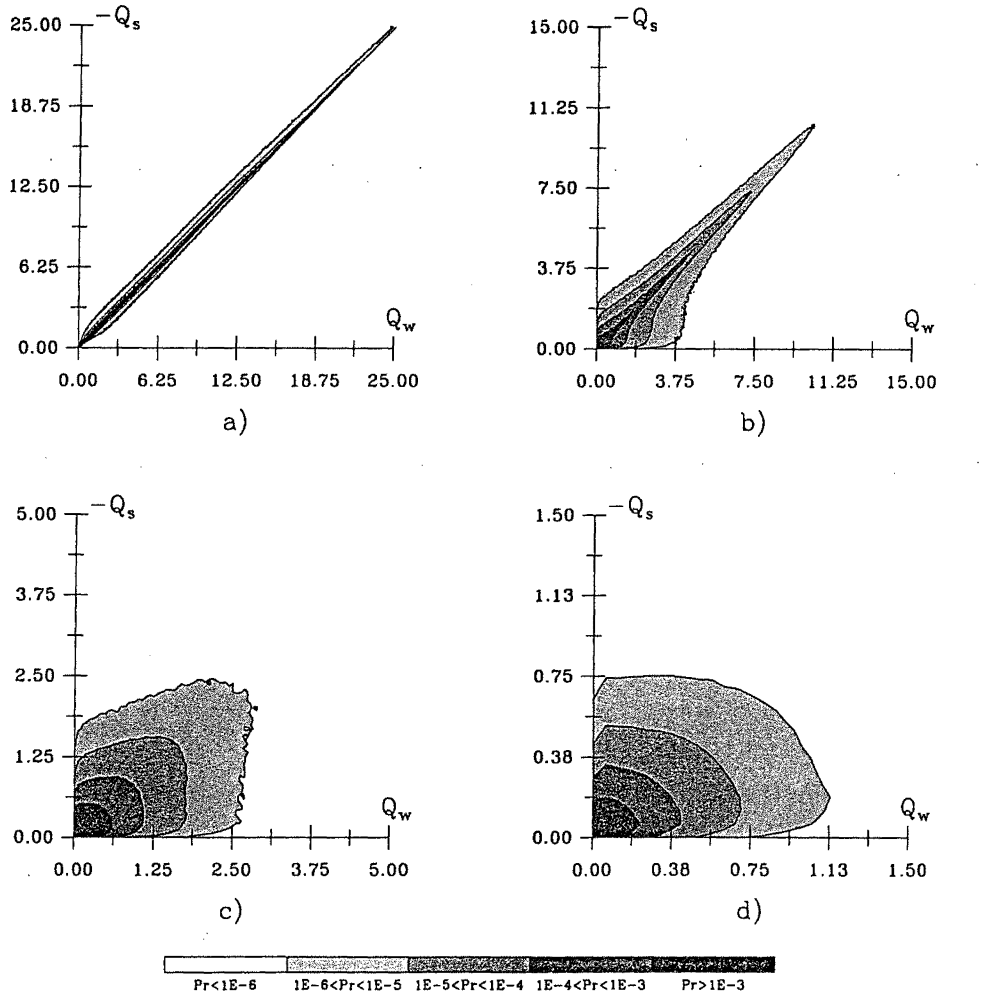

FIGURE 10. Joint probability density function between Q_W and $-Q_S$ for zero pressure gradient turbulent boundary layer flow with $R_\theta = 670$ in (a) viscous sublayer $y^+ < 5.0$ (b) buffer layer, $5.0 < y^+ < 41$, (c) logarithmic region, $41 < y^+ < 107$ and (d) wake region, $y^+ > 107$.

data close to the $-Q_s$ axis corresponds to irrotational rates of strain which cause dissipation. In Fig. 10(a) the sublayer results give sheet-like behavior which is not surprising. In Fig. 10(b), the buffer zone results are shown and there is a mixture of various types of motions, but vortex sheet behavior still dominates. Figure 10(c) shows a complete mixture of motion types and so also does Fig. 10(d). These results are consistent with the results of Blackburn *et al.* (1996).

Figure 11 shows the pdf between $|\sigma|\sigma/2$ and Q_w. Here

$$\sigma = \frac{\omega_i S_{ij} \omega_j}{\omega_k \omega_k} \tag{17}$$

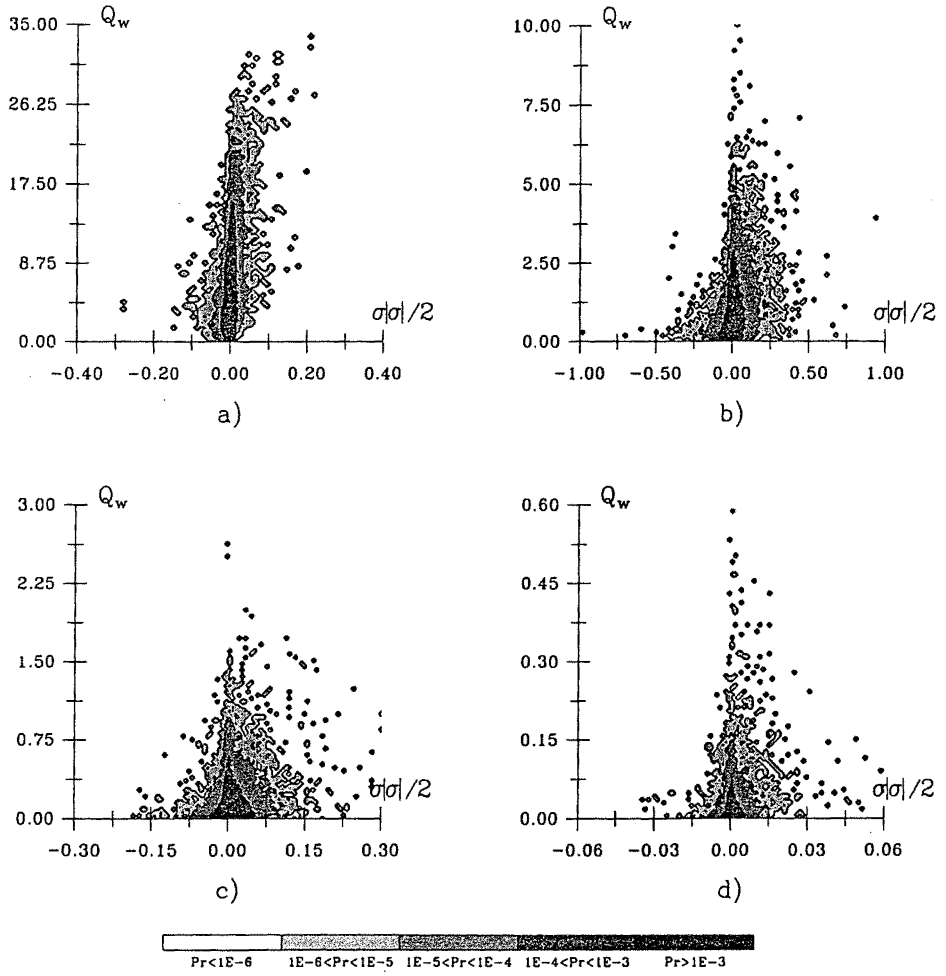

FIGURE 11. Joint probability density function between $|\sigma|\sigma/2$ and Q_W for zero pressure gradient turbulent boundary layer flow with $R_\theta = 670$ in (a) viscous sublayer $y^+ = 1.2$ (b) buffer layer, $y^+ = 16$, (c) logarithmic region, $y^+ = 87$ and (d) wake region, $y^+ = 243$.

where ω_i is the vorticity vector. Also it can be shown (e.g. see Soria and Chong (1993)) that

$$\omega_i S_{ij} \omega_j = R - R_s \tag{17}$$

The quantity $|\sigma|\sigma/2$ is a measure of the stretching and contracting in the direction of the vorticity vector. For all cases in Fig. 11 the highest vorticity has no stretching. Figure 12 shows the conditional volume integrated Q_w and Q_s for D greater than a specified threshold value as a function of this threshold value of D. These volume integrals have been normalized by the total volume integral of Q_w and Q_s respectively. In addition to the cases including the viscous zone, these normalized

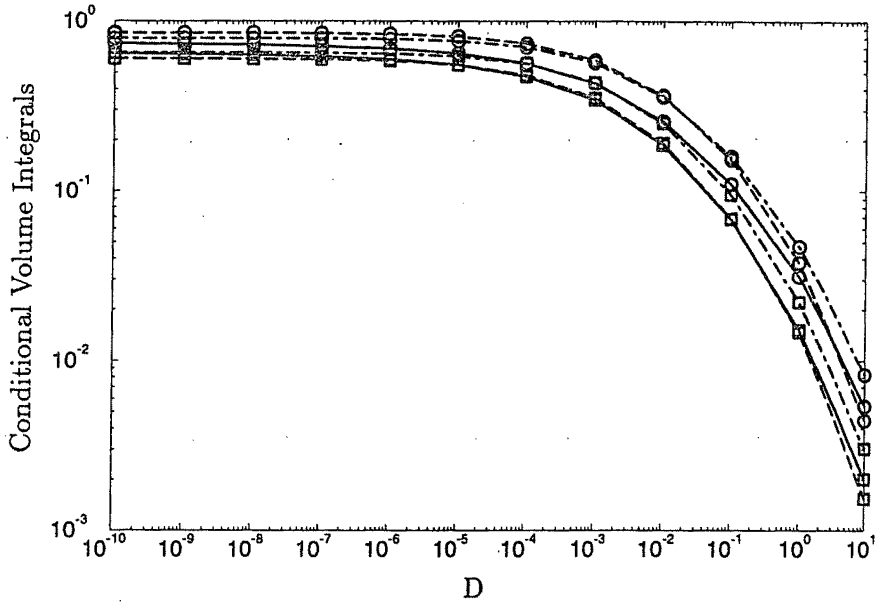

FIGURE 12. Conditional volume integrals of Q_s and Q_w normalized by the volume integrals of Q_s and Q_w respectively as a function of the cut-off value of the discriminant (D). —□— $\int Q_s(D > D_{given})dV / \int Q_s dV$. —○— $\int Q_w(D > D_{given})dV / \int Q_w dV$. —□—$\int Q_s(D > D_{given})dV / \int Q_s dV$ and $y^+ > 6.4$. —○—$\int Q_w(D > D_{given})dV / \int Q_w dV$ and $y^+ > 6.4$. --□- $\int Q_s(D > D_{given})dV / \int Q_s dV$ and $y^+ > 37$. --○- $\int Q_w(D > D_{given})dV / \int Q_w dV$ and $y^+ > 37$.

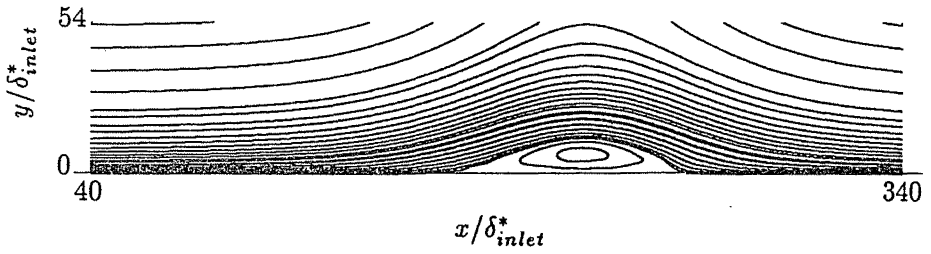

FIGURE 13. Mean streamline pattern for turbulent boundary layer with separation and reattachment. The dimensions shown were normalized by the displacement thickness at the inlet plane.

conditional integrals have been computed for $y^+ > 6.4$, thus eliminating the viscous sublayer contribution, and for $y^+ > 37.4$, thus eliminating the entire viscous zone contribution. The results show that independent of the y^+ threshold, focal regions account for approximately 75% of all volume integrated Q_w (i.e. enstrophy) and 66% of all volume integrated Q_s (i.e. dissipation of mechanical energy).

2.3 Separating and reattaching boundary layer

Figure 13 shows the mean flow streamlines of a turbulent boundary layer which nominally starts as a zero pressure gradient layer using the Spalart data of $R_\theta = 330$ as an inflow boundary condition. These computations were carried out using a finite differences method. As the flow moves downstream, the pressure gradient is arranged to be zero, then adverse, and then favorable, resulting in a separation bubble. The flow bears a strong resemblance to the experiment of Perry and Fairlie (1975), but the Reynolds number for that experiment was orders of magnitude higher than this computation.

Figure 14 (left side) shows an elevation view of the isosurfaces of the discriminant, and one can see a myriad of structures, many of which extend through from the wall to the outer edge of the boundary layer and generally lean in the streamwise direction. The structures leave the wall completely downstream of the mean separation point and ride over the separation bubble and then reattach. In the separation bubble there is an extensive region which seems to be devoid of fluid particles with positive discriminant. Figure 15 (left side) shows the instantaneous surface limiting streamlines or "skin friction lines". In the upstream part of the flow, bifurcation lines (curves towards which neighboring trajectories asymptote) are most evident. The precise definition and property of such lines are given by Hornung and Perry (1984) and Perry and Hornung (1984). As the pressure gradient becomes adverse, the skin friction lines reveal critical points all over the surface prior to the mean flow separation region. Under the bubble, the scale or spacing of the critical points is much larger than in the mean attached flow and large "nodes" of separation and reattachment are evident near the mean flow separation and reattachment "lines" respectively. After reattachment, bifurcation lines are reformed after a short streamwise distance with a much wider spanwise spacing than upstream of the separation bubble. This spacing is no doubt related to the viscous scaling as a lower shear velocity gives rise to the wider spacing.

Figure 15 (right side) shows the surface vortex lines which are orthogonal to the skin friction lines. In regions far upstream and downstream of the separation bubble, kinks in the vortex lines indicate a bifurcation line in the skin friction lines. Hornung and Perry (1984) showed that near a bifurcation line, neighboring skin friction lines are exponential curves and the vortex lines are orthogonal parabolas. Figure 16 shows skin friction lines and vortex lines superimposed for selected parts of the flow and the bifurcation patterns just mentioned are apparent. This orthogonality property throughout the limiting wall field acts as a useful check on the correctness in our data processing and in some aspects of the computations. Critical points in the limiting surface streamlines are also critical points in vorticity. In the separation region, the large velocity field nodes which are apparent are foci in the vorticity field.

In Figure 14, the side and plan views of the isosurfaces of the discriminant show that the structures appear to be pulled apart and stretched as they ride over the separation bubble. Coles (1956, 1957) formulated a hypothesis for the mean velocity profiles which considers a turbulent boundary layer to consist of two components superimposed - namely a wall component which follows the universal law of the

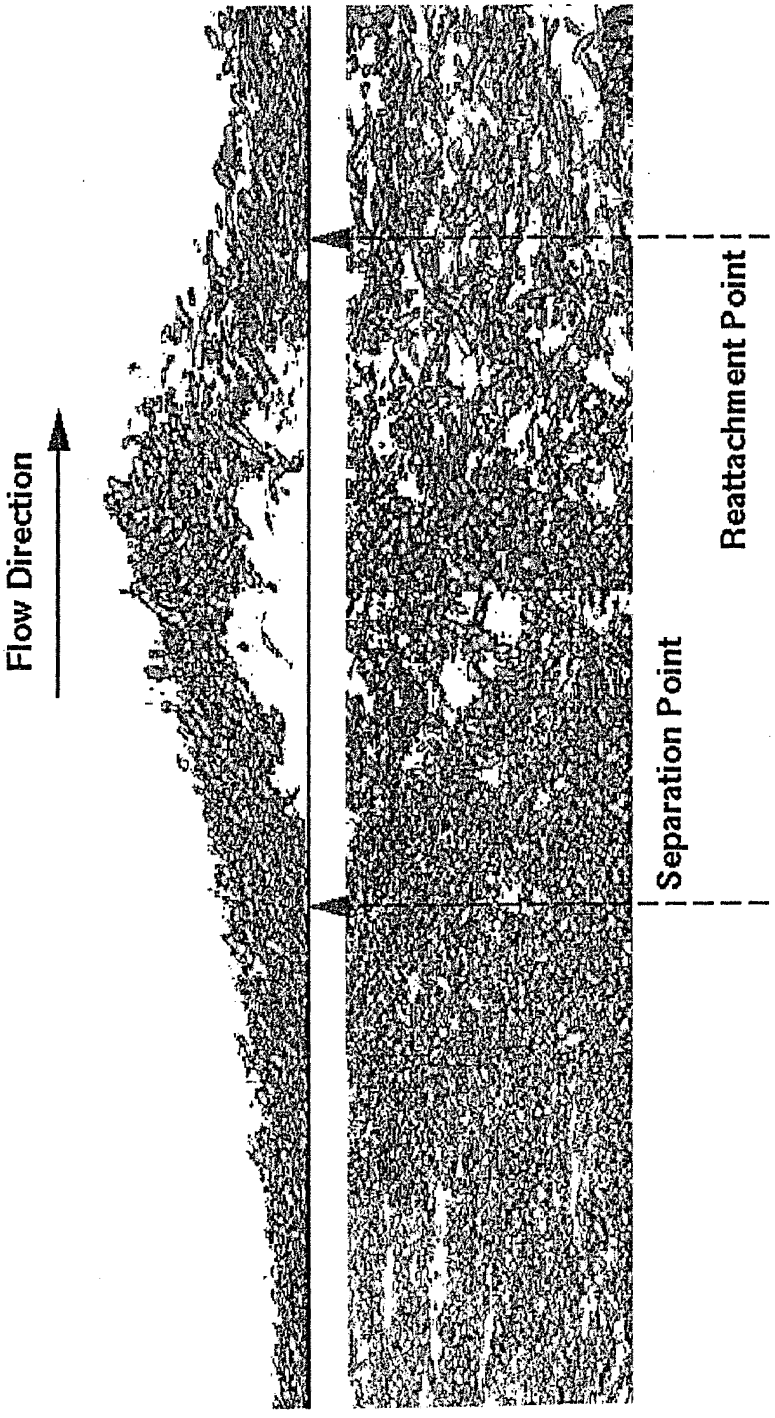

FIGURE 14. Isosurfaces of constant $D \sim 1$ to 10 showing focal structures in turbulent boundary layer with separation and reattachment from $x/\delta^*_{in} \approx 90$ to $x/\delta^*_{in} \approx 300$. Left) Elevation views. Right) Plan views.

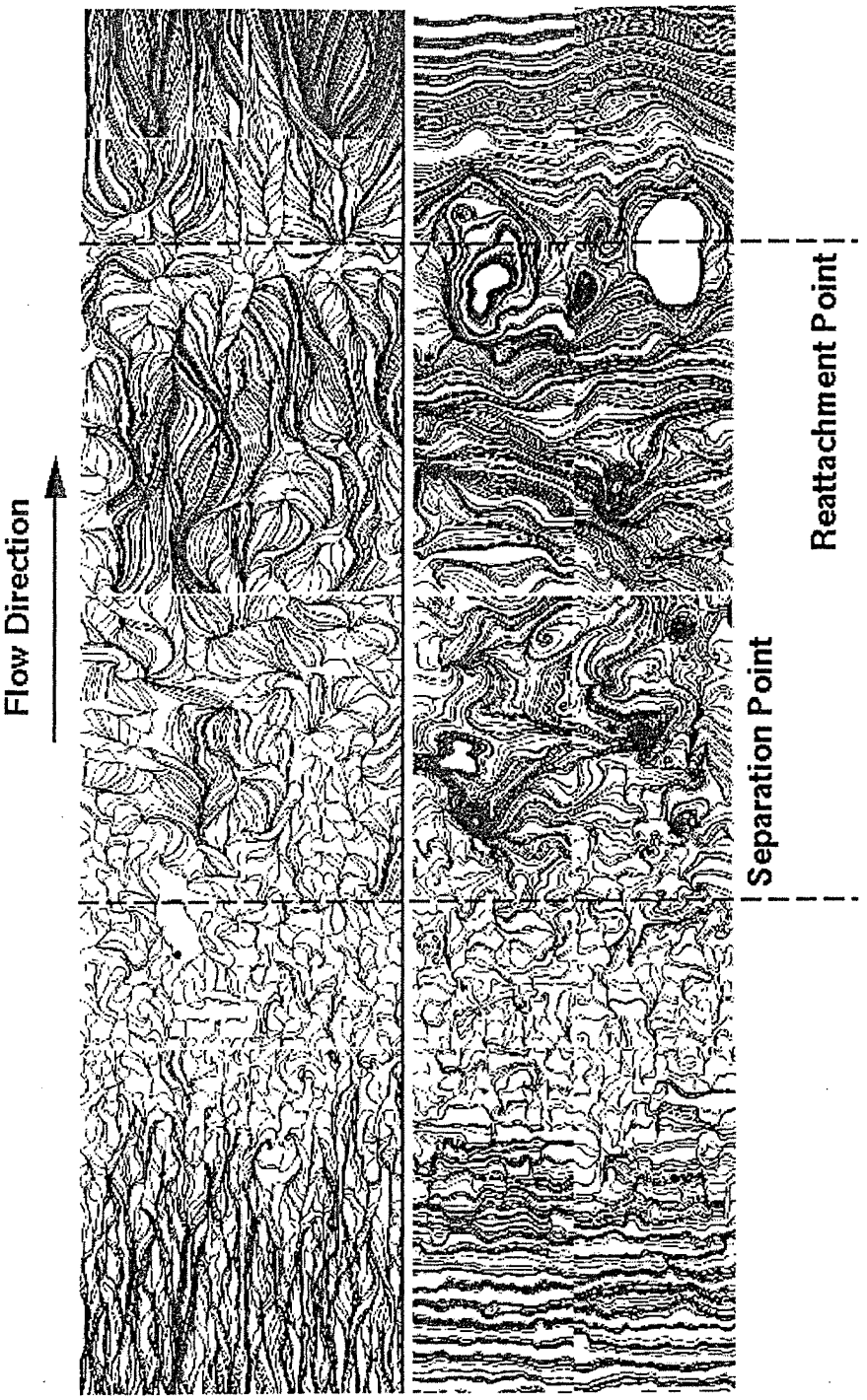

FIGURE 15. Skin-friction lines and surface vorticity lines from $x/\delta^*_{in} \approx 90$ to $x/\delta^*_{in} \approx 300$. Left) Skin-friction lines. Right) Vorticity lines.

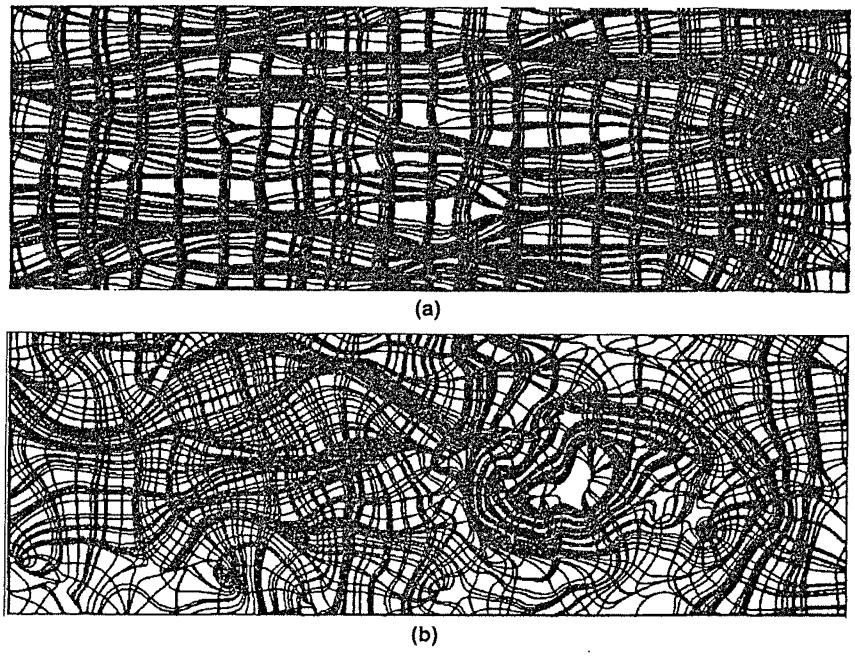

FIGURE 16. (a) and (b). Skin-friction lines and surface vorticity lines superimposed. (a) Unseparated region. (b) Separated region.

wall and a wake component which follow a universal law of the wake. Recently this has been extended to include the turbulence structure by Perry and Marusic (1995) and Marusic and Perry (1995) where the wall component for both mean flow and Reynolds stress is considered to be generated by wall attached eddies where the vortex lines connect to the wall like the Theodorsen type eddies as shown sketched in Fig. 17(a). The wake component of velocity and the peak in the Reynolds shear stress which occurs well away from the wall when the Coles wake factor is appreciable is considered to be generated by wake eddies which are thought to consist of spanwise undulating vortex cores as shown in Fig. 17(b). This model is supported by mean flow, broadband turbulence and spectral measurements and an analysis using convolution integrals for computing the effect of a random array of eddies with a range of scales (see Perry & Marusic (1995) for details). It is almost obvious from the picture of the isosurface of the discriminant in Fig. 14 that as the flow develops in the adverse pressure gradient and as the Coles wake factor increases, more of the eddies which contribute to the Reynolds shear stress and mean flow vorticity are eddies which are not connected to the boundary. Once separation has occurred, there are no eddies connected with the wall. Unfortunately, memory limitations of the flow visualization software prevented a full rendering of the details of the flow field causing the isosurfaces to appear lumpy and unstructured. More work on this is required.

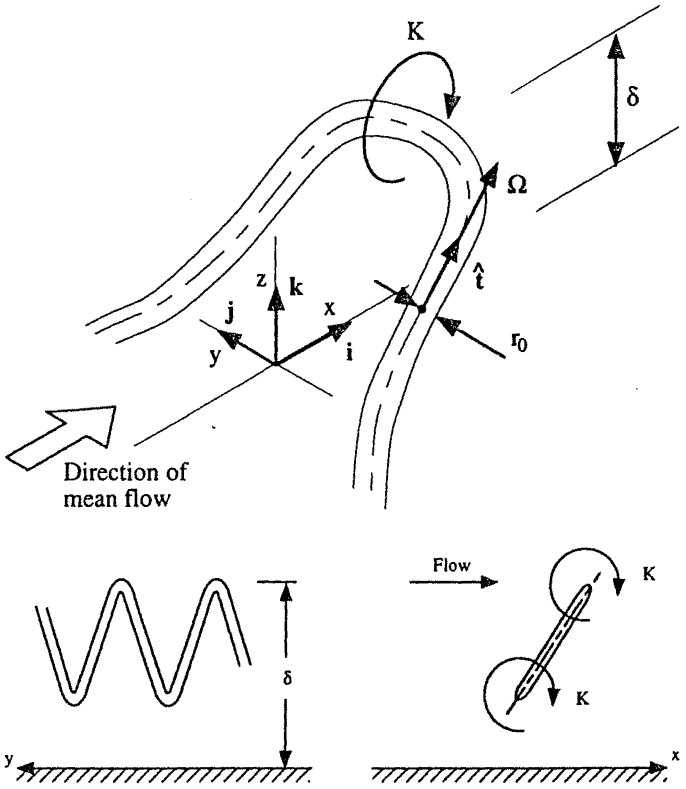

FIGURE 17. (a) Wall eddies and (b) wake eddies, after Perry & Marusic (1995). Note that here, unlike earlier convention, z is the coordinate normal to the wall rather than y.

3. Conclusions

This study has shown that there exists evidence for the Reynolds shear stress carrying structures in zero pressure gradient turbulent boundary layers, and they consist of attached eddies in the form of tubes of positive discriminant connected to the wall. The vortex loops envisioned by Theodorsen, the vortex tubes used in the model of Perry and Marusic (1995), and the tubes or arches of positive discriminant observed in simulations all bear striking resemblance to one another. But there are important differences which still need to be reconciled. The evidence presented here indicates that Reynolds stress generation is correlated, not with the vorticity, but with the discriminant of the velocity gradient tensor, especially near the wall where these two quantities have quite different character.

For adverse pressure gradients, there is evidence of wake structures which are not connected to the wall. However, because of the early stages of the present work and the difficulties encountered with the resolution of the stored data (if not the computed data), the evidence, although encouraging, is not conclusive. Furthermore we should keep in mind at all times that we are dealing with low Reynolds number flows where the range of eddy length scales is relatively small.

Acknowledgments

This work was supported by the Center for Turbulence Research, NASA AMES-Stanford Joint Institute for Aeronautics and Acoustics, NASA Grant NAG-1-1610 and the Australian Research Council. Additional supercomputing resources were provided by the San Diego Supercomputer Center.

REFERENCES

BLACKBURN, H. M., MANSOUR, N. N. & CANTWELL, B. J. 1996 Topology of fine-scale motions in turbulent channel flow. *J. Fluid Mech.* **310,** 269-292.

CANTWELL, B. J. 1979 Coherent turbulent structures as critical points in unsteady flow. *Archiwum Mechaniki Stosowanej. (Archives of Mechanics).* **31, 5,** 707-721.

CANTWELL, B. J. 1992 Exact solution of a restricted Euler equation for the velocity gradient tensor. *Phys. of Fluids.* **4(4),** 782-793.

CHACIN, J. M., CANTWELL, B. J. & KLINE, S. J. 1996 Study of turbulent boundary structure using the invariants of the velocity gradient tensor. To appear in the *Journal of Experimental, Thermal and Fluid Science.* **November.**

CHONG, M. S., PERRY, A. E. & CANTWELL, B. J. 1989 A general classification of three-dimensional flow fields. *Proceedings of the IUTAM Symposium on Topological Fluid Mechanics, Cambridge* (Edited by H. K. Moffatt and A. Tsinober), 408-420.

CHONG, M. S., PERRY, A. E. & CANTWELL, B. J. 1990 A general classification of three-dimensional flow fields. *Phys. of Fluids.* **A4(4),** 765-777.

DALLMANN, U. 1983 Topological structures of three-dimensional flow separations. *DFVLR Rep. IB 221-82-A07.* Gottingen, West Germany.

HORNUNG, H. G. & PERRY, A. E. 1984 Some aspects of three-dimensional separation. Part I. Streamsurface bifurcations. *Z. Flugwiss. Weltraumforsch.* **8,** 77-87.

JEONG, J. & HUSSAIN, F. 1995 On the identification of a vortex. *J. Fluid Mech.* **285,** 69-94.

KIM, J. 1989 On the structure of pressure fluctuations in simulated turbulent channel flow. *J. Fluid Mech.* **205,** 421-451.

LUGT, H. J. 1979 The dilemma of defining a vortex. In *Recent Developments in Theoretical and Experimental Fluid Mechanics* (ed. U. Muller, K.G. Roesner & B. Schmidt), Springer, 309-321.

MARTIN, J. & DOPAZO, C. 1995 Velocity gradient invariant evolution from a linear diffusion model. *Proceedings of the Twelfth Australasian Fluid Mechanics Conference.* 743-746.

MARUSIC, I. & PERRY, A. E. 1995 A wall-wake model for the turbulent structure of boundary layers. Part 2. Further experimental support. *J. Fluid Mech.* **298,** 389-407.

NA, Y. & MOIN, P. 1996 Direct numerical simulation of turbulent boundary layers with adverse pressure gradient and separation. *Stanford University Report TF-68.*

PERRY, A. E. & FAIRLIE, B. D. 1975 A study of turbulent boundary-layer separation and reattachment. *J. Fluid Mech.* **69,** 657-672.

PERRY, A. E. & CHONG, M. S. 1982 On the mechanism of wall turbulence. *J. Fluid Mech.* **119,** 173-217.

PERRY, A. E. & HORNUNG, H. G. 1984 Some aspects of three-dimensional separation. Part II. Vortex skeletons. *Z. Flugwiss. Weltraumforsch.* **8,** 155-160.

PERRY, A. E., HENBEST, S. M. & CHONG, M. S. 1986 A theoretical and experimental study of wall turbulence. *J. Fluid Mech.* **165,** 163-199.

PERRY, A. E. & MARUSIC, I. 1995 A wall-wake model for the turbulent structure of boundary layers. Part 1. Extension of the attached eddy hypothesis. *J. Fluid Mech.* **298,** 361-388.

ROBINSON, S. K. 1991 Coherent motions in the turbulent boundary layer. *Ann. Rev. Fluid Mech.* **23,** 601-639.

SORIA, J., CHONG, M. S., SONDERGAARD, R., PERRY, A. E. & CANTWELL, B. J. 1992 Topology of time-developing incompressible mixing layers. *Proceedings of the Center for Turbulence Research Summer Program, 1992.* Stanford Univ./NASA Ames, 101-121.

SORIA, J. & CHONG, M. S. 1993 The structure of intense focal regions in a direct numerical wake flow calculation. *Proceedings of the Ninth Symposium on Turbulent Shear Flows.* 3.1.1-3.1.6.

SORIA, J., CHONG, M. S., SONDERGAARD, R., PERRY, A. E. & CANTWELL, B. J. 1994 A study of the fine scale motions of incompressible time-developing mixing layers. *Phys. of Fluids.* **6(2),** 871-884.

SPALART, P. R. 1988 Direct simulation of a turbulent boundary layer up to Re_θ = 1410. *J. Fluid Mech.* **187,** 61-98.

THEODORSEN, T. 1955 The structure of turbulence. *50 Jahre Grenzschichtforsung.*

TOWNSEND, A. A. 1976 *The Structure of Turbulent Shear Flow* 2nd edn. Cambridge University Press.

TRUESDELL, C. 1954 *The Kinematics of Vorticity. Indiana University Press.*

VIEILLEFOSSE, P. 1982 Local interaction between vorticity and shear in a perfect incompressible fluid. *J. Phys. (Paris).* **43,** 837-842.

VIEILLEFOSSE, P. 1984 Internal motion of a small element of fluid in an inviscid flow. *Physica A.* **150,** 150-162.

VOLLMERS, H. 1983 Separation and vortical-type flow around a prolate spheroid. Evolution of relevant parameters. *AGARD Symposium on Aerodyn. of Vortical Type Flow in Three-Dimensional. Rotterdam.* **AGARD-CP342,** 14.1-14.14.